Impacts of Subauroral Polarization Streams on Storm-Enhanced Density and Tongue of Ionization

Shuhan Li[1], Jing Liu[1], Wenbin Wang[2], Jun Liang[3] and Kedeng Zhang[4]

[1]Shandong Provincial Key Laboratory of Optical Astronomy and Solar-Terrestrial Environment, School of Space Science and Physics, Institute of Space Sciences, Shandong University, Weihai, Shandong, China,

[2]High Altitude Observatory, National Center for Atmospheric Research, Boulder, Colorado, USA,

[3]Department of Physics and Astronomy, University of Calgary, Calgary, Alberta, Canada,

[4]Department of Space Physics, School of Electronic Information, Wuhan University, Wuhan, China.

Key Points:

- Subauroral polarization streams (SAPS) tend to move storm-enhanced density (SED)/tongue of ionization (TOI) westward.
- SAPS reduce the intensity of TOI.
- SED/TOI is affected by changing ionospheric loss rates and horizontal westward E×B transports.

*Corresponding author: Liu J., **liujing2019@sdu.edu.cn**

Abstract

The influences of subauroral polarization streams (SAPS) on storm-enhanced density (SED) and tongue of ionization (TOI), an important topic in the field of magnetosphere-ionosphere-thermosphere coupling, however, remain undetermined. The Thermosphere-Ionosphere-Electrodynamics General Circulation Model (TIEGCM) with/without an empirical SAPS model has been used to investigate the impacts of SAPS on SED and TOI. The modeled TEC and ion drift velocities agree reasonably well with the observations of GNSS and DMSP satellites on 17 March 2013. The TIEGCM simulations show that SAPS can significantly affect the electron density of SED and TOI depending on the relative location of SAPS and SED. SAPS reduces the electron density at the eastward edge of SED where they are overlapped, and enhances SED at its westward edge. A term-by-term analysis of the O^+ ion continuity equation in the F-region shows that the electron density depletions at the eastward edge of SED are mainly due to increased local plasma loss rates because of SAPS elevated plasma-neutral temperatures and O/N_2 reduction because of thermosphere upwelling. The electron density enhancements in the westward edge of SED are mainly due to SAPS-induced westward plasma E×B transports and O/N_2 increment because of thermospheric downwelling. Moreover, SAPS-induced electron depletions in the throat region weaken TOI as plasmas undergo anti-sunward convection into the polar cap.

Plain Language Summary

Subauroral polarization streams (SAPS), storm-enhanced density (SED) and tongue of ionization (TOI) are prominent structures in subauroral and polar ionosphere during geomagnetic storm. The effects of SAPS on SED and TOI remains controversial. In this work, the simulated results from Thermosphere-Ionosphere-Electrodynamics General Circulation Model (TIEGCM) with and without SAPS empirical model are compared to understand the impacts of SAPS. The modeled

results indicate that SAPS tend to move SED and thus TOI throat regions towards the morning side, and weaken TOI in the polar cap. Further analyses show that SAPS enhanced plasma and neutral temperatures lead to thermosphere upwelling/downwelling and thus weaken/intensify the eastward/westward edge of SED because of modified chemical reaction rates. In addition, the gradients of SAPS-induced westward E×B drift also transport additional plasma from eastside to westside of SED.

1. Introduction

Ionospheric subauroral polarization streams (SAPS) (Galperin et al., 1974; Karlsson et al., 1998; Smiddy et al., 1977; Spiro et al., 1979) refer to intense westward plasma flows driven by enhanced poleward electric fields in the dusk sector of the subauroral region. The term “SAPS” is proposed by Foster and Burke (2002a) to include subauroral westward plasma flows in a wider latitude region and narrower and more intense plasma jets (PJ) (Galperin et al., 1974) or subauroral ion drifts (SAID) (Anderson et al., 1993; Spiro et al., 1979). The average peak ion velocities of SAPS are larger than 500 m/s and located on the equatorward boundary of particle precipitation (Foster and Vo, 2002b). The occurrence of SAPS in ionosphere is related to the enhanced poleward electric fields in the duskside midlatitude trough region with low conductivities, probably caused by the mapping of magnetospheric electric field (Southwood and Wolf, 1978) or the field aligned current continuity (Anderson et al., 1993). The friction between high-speed SAPS and neutral atmosphere tends to heat the plasmas and deplete electron density and conductivity (Schunk et al., 1975), and this positive feedback effect strengthens the SAPS (Wolf et al., 2007). But some theoretical works show the electric fields are hard to penetrate the plasma and induce ion drift (Tu et al., 2008; Vasyliunas, 2001). The formation of SAPS electric fields related with magnetosphere-ionosphere-thermosphere (M-I-T) coupling remains a problem. Considering the morphological and physical characteristics of SAPS which can reflect the state of M-I-T coupling

(Goldstein et al., 2005; He et al., 2018; Horvath et al., 2020; Wang et al., 2012; Zhang et al., 2017; Zou et al., 2009), SAPS and related effects are interesting topics in M-I-T coupling studies.

In addition to SAPS, other prominent ionosphere structures exist in the subauroral latitude during geomagnetic storms. A significant electron density enhancement often occurs in the afternoon and dusk sector during a geomagnetic storm, called storm-enhanced density (SED) (Foster et al, 1993, 2007b, 2021; Liu et al., 2016a, 2016b; Zou et al., 2013, 2014). SED is related to the high-latitude convection and located at the equatorward edge of the middle latitude ionospheric electron density trough (Foster et al., 1993). The density enhancements of SED are localized with large density gradients at its boundaries to form ionospheric irregularities (Coster and Skone, 2009; Sun et al., 2013). SED often extends northwestward to higher latitudes and form a narrow plume. This plume can be further carried by the anti-sunward convection flows into the polar cap. The continuous high-density structure is termed the tongue of ionization (TOI) (Foster et al., 2005; Hosokawa et al., 2010; Liu et al., 2015), while the discrete structures are named patches (Moen et al., 2013). Therefore, TOI is influenced not only by the two-cell convective pattern, but also by the characteristics of SED located in the throat region of TOI. It should be noted that SED are not always accompanied by SAPS which can also be observed in quiet time (e.g., He et al., 2017; Kunduri et al., 2017; Lejosne and Mozer, 2017) and may be related to substorms (He et al., 2017). But when SAPS and SED occur together in a geomagnetic storm, considering that the occurrence of SED region often overlaps with that of SAPS, SAPS may influence the formation and development of SED structures, and thus the TOI structures (Foster and Rideout, 2007a).

Many observations from satellites and incoherent scattering radar revealed that the location of SAPS coincided with middle latitude ionospheric F region plasma density trough (e.g., Anderson et al., 1993; Foster et al., 2007b; Spiro et al., 1979). To simulate SAPS effects, Sellek et al. (1991) and Moffett et al. (1992) imposed an extra high-speed westward ion drift at subauroral latitudes, and Pintér et al. (2006)

imposed a poleward electric field in pre-midnight sector at 50-60° magnetic latitude into the Sheffield Coupled Thermosphere-Ionosphere-Plasmasphere (CTIP) model. Their results showed that the friction between the rapid plasma flow and thermosphere can enhance the ion temperature, elevating recombination rates and decreasing plasma densities in F region. Some researchers thus considered the density depletions induced by SAPS against the formation of SED (e.g., Fuller-Rowell, 2011). However, a different viewpoint was thought the strong sunward ion flux carried by SAPS to be a source of SED (Foster et al., 2007b; Erickson et al., 2011; Park et al., 2012). SAPS was also considered to have a close association with SED plume and plasmasphere erosion (Foster et al., 2007b; Horvath et al., 2009). Horvath et al. (2014) showed that SAPS electric field could enhance the process of plasmaspheric erosion and provide a continuous supply of high-density SED plume plasma to develop and maintain SEDs during the main phase. Lu et al. (2020) compared TIEGCM model and GNSS TEC to confirm that SAPS contribute to form SED plume at the equatorward and westward edge of the SAPS channel.

To sum up, there is still no clear explanation for the contradiction between SAPS causing reduced density and contributing to SED. The dominate mechanism of the interaction between SAPS and SED are not fully understood in typical storm events. These impair our understanding of subauroral electrodynamics and dynamics and even the related M-I-T coupling processes during geomagnetic disturbed conditions. The impacts of SAPS can alter the SED edges with high-density gradients associated with irregularity production and scintillation (Basu et al., 2007; Foster and Rideout, 2005). Their interaction can thus disrupt the civilian and military electromagnetic signals in subauroral region.

In this work, the impacts of SAPS flow on SED and TOI have been investigated by comparing the results between TIEGCM with and without SAPS empirical model. Then the contribution of each physical mechanism is explored using term-by-term analysis method.

2. Model and Data

The NCAR Thermosphere-Ionosphere-Electrodynamics General Circulation Model (TIEGCM) is a first-principles three-dimensional model, which self-consistently solves the continuity, momentum and energy equations for ion and neutral species. TIEGCM is driven by solar EUV and UV parameterized by $F_{10.7}$ solar index (Richards et al., 1994), particle precipitation (Roble and Ridley, 1987) obtained from 3-hour Kp index, high-latitudes convection electric fields provided by Heelis model (Heelis et al., 1982) or Weimer model (Weimer, 2005), and diurnal and semidiurnal migrating/non-migrating tides (Hagan and Forbes, 2002, 2003) specified by the Global Scale Wave Model (GSWM). The high-resolution TIEGCM used in this study is 2.5° in latitude and longitude and one quarter of a scale height in the vertical pressure coordinate ranging from ~97 to ~600 km.

In this work, the SAPS effects are introduced into TIEGCM by imposing the SAPS ion drift velocity into the subauroral region at all altitudes, referring to as SAPS-TIEGCM. In the following part, TIEGCM without SAPS imposed is named as default-TIEGCM. In SAPS-TIEGCM model, the 3-hour Kp index is used to drive empirical SAPS model and high-latitude Heelis model, including convection and auroral particle precipitation pattern. SAPS model is called for the grid points within 10° equatorward from the auroral precipitation boundary at each time step. The calculated horizontal ion drift velocities are added to the ion velocities obtained from default-TIEGCM as the modification of SAPS. Then the modified E×B drift is substituted into the self-consistent I-T system. The same model has also been used in the researches of the ionosphere-thermosphere response to SAPS (Wang et al., 2012; Zhang et al., 2021a, 2021b, 2022). For the purpose of analyzing the effects of SAPS on SED and TOI, the results from default-TIEGCM and SAPS-TIEGCM are compared in this work.

The solar wind parameters, interplanetary magnetic field, and geomagnetic activity index are obtained from the OMNI database. MIT's Madrigal database provides the global ionospheric TEC data, which is the vertical height integral of

electron density with 1°×1° horizontal resolution every 5 min distributed over locations where GPS data is available (Rideout et al., 2006). In this work, a median filtering for TEC is used to reduce its noise. The ion drift velocities are observed by ion drift meters of DMSP satellites (Rich et al., 1994). The horizontal cross-track ion drift velocity is projected to zonal direction to compare with the simulated results.

3. Results

3.1. Interplanetary solar wind and geomagnetic activity conditions

The geomagnetic storms significantly perturbed the geospace system during the St. Patrick's Days of 17 March 2013 (Li et al., 2014; Foster et al., 2014a, 2014b; Liu et al., 2016b; Zhang et al., 2017). Figure 1 shows the temporal variations of interplanetary magnetic field (IMF) B_z and B_y components in GSM coordinates, solar wind velocity V_s, the symmetric ring current (SYM-H) index, the AE index, and the Kp index during DOY 75-77 (Mar 16-18), 2013. The shaded region at 1700-2300 UT on DOY 76 is the interval of the SED and TOI.

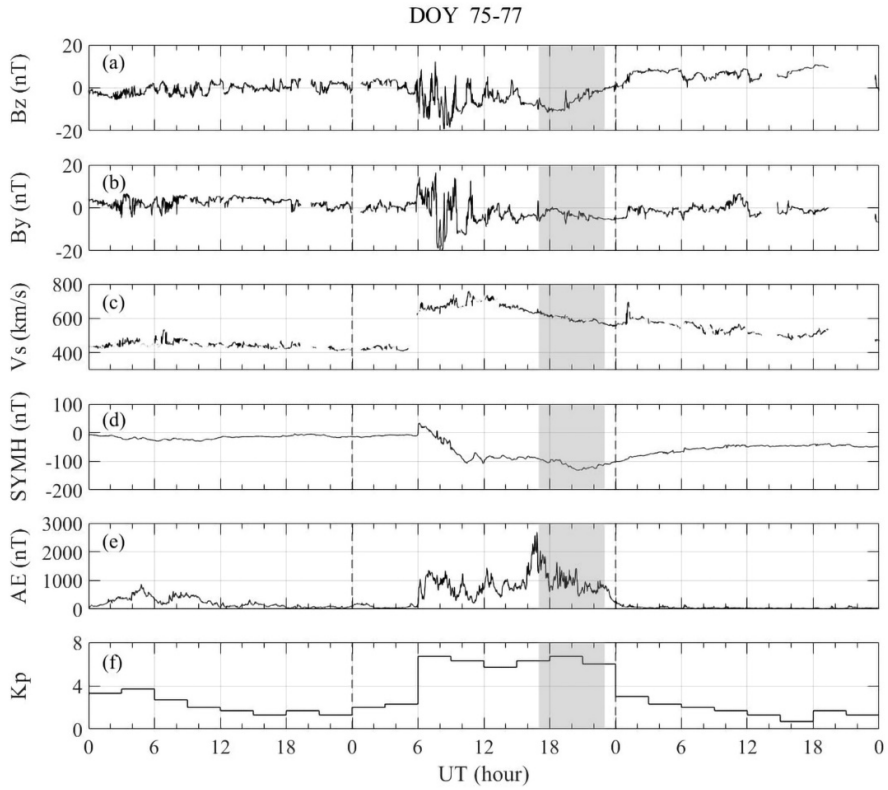

Figure 1. (a,b) IMF B_z, B_y, (c) solar wind velocity V_s, (d,e,f) SYM-H, AE, and Kp index from DOY 75 to 77 (March 16 to 18), 2013. The shaded regions denote the interval of SED and TOI.

On DOY 76 a strong disturbance of IMF and a sudden enhancement in the solar wind velocity approximately at 0600 UT indicate an interplanetary disturbance arriving the magnetosphere. In the subsequent geomagnetic storm, the SYM-H index reaches the minimum values of -100 nT and -132 nT at ~1000 UT and ~2000 UT, respectively. The AE index increases to a maximum value of 2689 nT at 1648 UT in the main phase of storm. SED and TOI were observed at 1700-2300 UT, which locates at the later main phase and early recovery phase of the geomagnetic storm as reported in previous studies (Ferdousi et al., 2019; Lin et al., 2019; Liu et al., 2016b; Yu et al., 2015).

3.2 Comparisons of TEC and ion horizontal drift velocities

Figure 2 shows the polar view of absolute TEC difference (ΔTEC) in the Northern Hemisphere between storm (DOY 76) and quiet (DOY 75) times from GNSS, SAPS-TIEGCM, and default-TIEGCM during 1600-2200 UT. In the snapshot of Figures 2a-d, a GNSS-observed TEC enhancement forms below 50°N around the duskside at 1600-2000 UT, and ΔTEC recovers gradually during 2000-2200 UT. An obvious SED plume with an intensity of ~5 TECU appears at 1300-1400 LT at 2000 UT. The modeled SED in ΔTEC also occurs at the throat region at 1300-1400 LT, with an overestimated magnitude of ~6 TECU (Figures 2e-h). The overestimation of dayside TEC is perhaps owing to the underestimated Joule Heating, and the resultant smaller loss rate, or excess soft particle precipitation (Liu et al., 2016b). Both in the observations and results from SAPS-TIEGCM (Figures 2a-h), a TEC depletion appears at geographic latitudes of 50-70°N in the dusk sector, with an intensity of ~-6 TECU. Previous studies have disclosed that the trough of ΔTEC due to SAPS extends sunward and tended to cut off the TOI structure (Horvath et al., 2016; Zheng et al., 2008). Compared with the results from default-TIEGCM (Figures 2i-l), the trough structures at dusk of subauroral latitudes simulated by SAPS-TIEGCM (Figures 2e-h) are more aligned with the observations (Figures 2a-d) in a strong SAPS case. Considering the only modification in SAPS-TIEGCM is the additional ion drift velocity, thus the differences between modeled TEC by SAPS-TIEGCM and default-TIEGCM are caused by SAPS directly or indirectly.

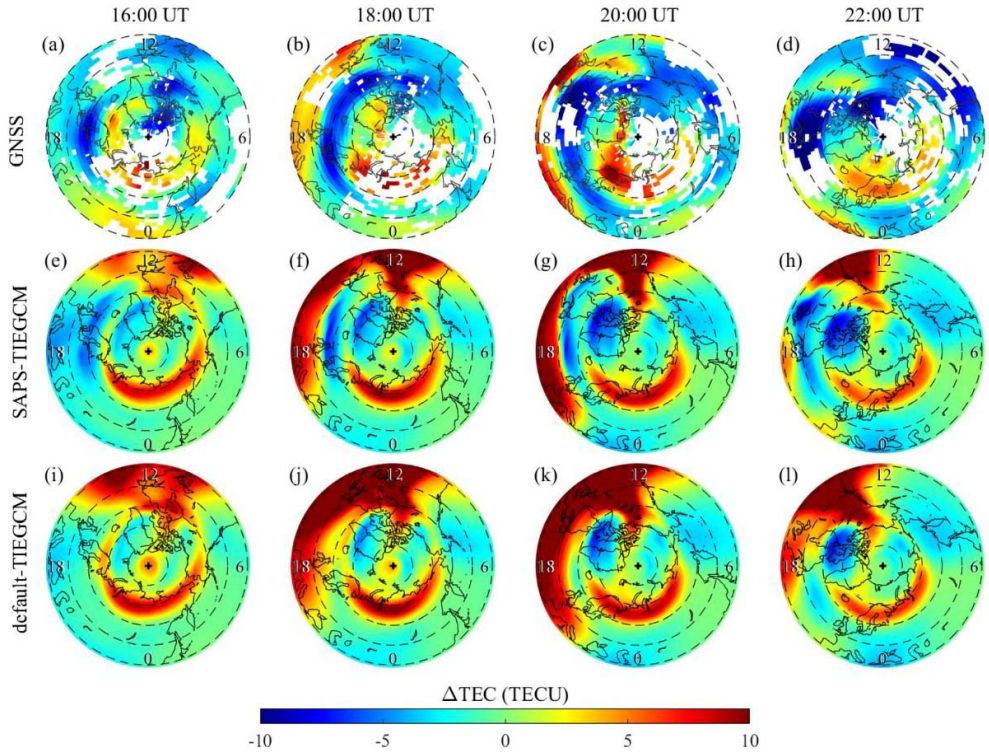

Figure 2. Absolute TEC difference in the Northern Hemisphere between storm time (DOY 76) and quiet time (DOY 75) from GNSS (a-d), SAPS-TIEGCM (e-h) and default-TIEGCM (i-l), respectively. The dotted circles are geographic 10° apart with the outer circle at 40°N.

Figures 3a and 3b show the modeled eastward ion drift velocities from default-TIEGCM and SAPS-TIEGCM on pressure level 2.0 (~300 km) at 2200 UT, respectively. The observed cross-track velocities from DMSP F17 at 2140-2210 UT are overlapped. The detailed profiles of simulations and observation on DMSP trajectory are shown in Figure 3c. Since the magnetic field lines at high-latitudes are nearly vertical, the simulated horizontal ion drift velocities on ~300 km are considered to be approximately equal to the measurements of DMSP satellite on ~830 km. An obvious two-cell plasma convection is presented in Figure 3a. The differences between the modeled ion velocities from default-TIEGCM and SAPS-TIEGCM are mainly located in the dusk subauroral region in Figures 3a and 3b. Comparing with Figure 3a, Figure 3b shows a stronger westward ion drift with a

peak velocity of over 1000 m/s located at ~50° in dusk sector at 2200 UT. The detailed profile in Figure 3c indicates that the simulated SAPS-induced westward flow velocity is ~1100 m/s at the equatorward of the high-latitude evening convection, and it is consisted with the DMSP observations in magnitude. The simulation results underestimate the size of the convection pattern calculated by empirical Heelis model driven by 3-hour Kp, and it makes the simulated convection velocity peak in both dusk and dawn shrink to higher latitude. However, considering the better simulated results of TEC and SAPS velocity from SAPS-TIEGCM than that from default-TIEGCM (Figures 2 and 3), SAPS-TIEGCM model can be used to analyze the dynamics and electrodynamics processes induced by SAPS qualitatively (Wang et al., 2012; Wu et al., 2019; Zhang et al., 2021a).

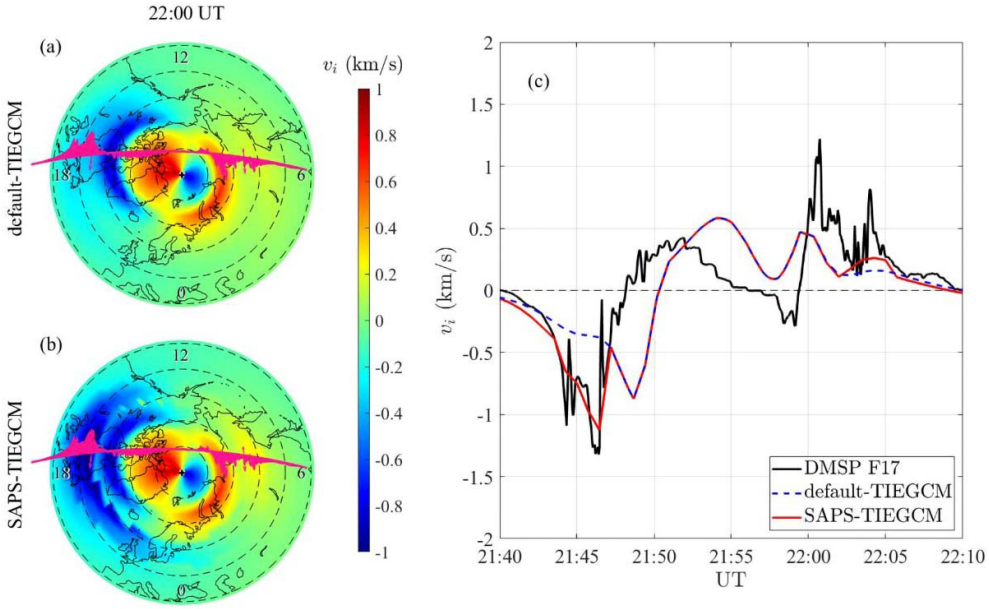

Figure 3. (a,b) Polar view of eastward ion drift velocities on pressure level 2.0 (~300 km) in the Northern Hemisphere at 2200 UT on DOY 76 (Mar. 17, 2013) from default-TIEGCM and SAPS-TIEGCM. Overlapping magenta arrows show DMSP F17 cross-track ion velocities during 2140-2210 UT. (c) Detailed eastward ion drift velocities on the track of DMSP satellite.

3.3 Effects of SAPS on SED and TOI

Figure 4 illustrates the absolute TEC difference between TIEGCM with and without SAPS model. The locations of SAPS channel are shown as the orange lines, which are the contour lines where the ion westward velocity difference between SAPS-TIEGCM and TIEGCM exceeds 200 m/s. The contour lines of SED and the peak of TOI with and without SAPS effects are respectively painted green and purple. In Figure 4, TEC depletions locate around SAPS channel with a TEC reduce of ~12 TECU, while a TEC enhancement of ~6 TECU appears at the westward edge of SAPS channel. These SAPS-induced variations cause the westward movement of SED and TOI peak, which is more obvious (~10° longitude) in Figures 4b and 4c. It indicates that the values of SED/TOI westward shift increase with the development and persistence of SAPS.

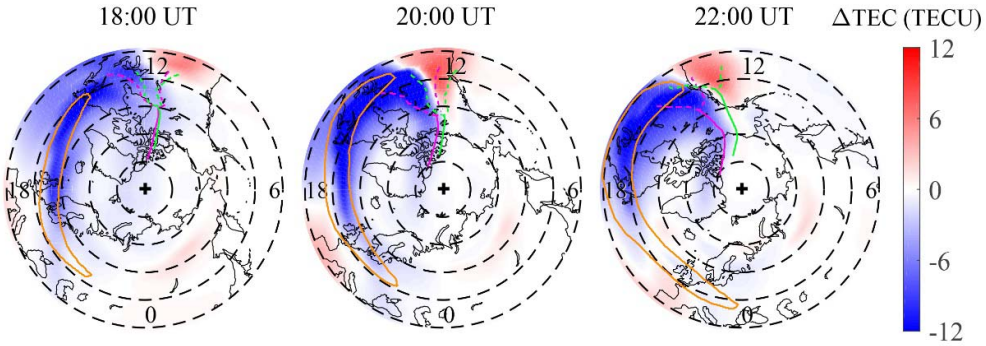

Figure 4. Absolute TEC difference between SAPS-TIEGCM and TIEGCM on DOY 76. The orange lines denote the locations of SAPS. The dashed and solid lines indicate the locations of SED and TOI peak, while the purple and green lines are for TIEGCM and SAPS-TIEGCM respectively.

SAPS-induced local TEC reduce along its flow channel has been reported by Schunk et al. (1975), Foster et al. (2002a), and Wang et al. (2012). It is worth noting that the electron density depletions on the westward edge of SAPS are more significant than that on its eastward edge. As the enhanced westward transports are determined by the gradients of increased westward ion drift velocities, the heated

plasmas move from dusk to post-noon and tend to accumulate at the westward edge of SAPS. The stacked heated plasmas with higher loss rates thus tend to reduce more electron density at westside of SAPS along its channel. SAPS can thus reduce TEC in eastward edge of SED region and throat region of TOI. Subsequently, the effects of reducing electron density diffuse at the westward edge of SAPS and enter the polar cap with sunward return convection to weaken the peak of TOI. However, in the noon sector where SAPS no longer have high drift velocities, a promotion of TEC appears at the westward edge of SAPS channel. Therefore, the impacts of SAPS on SED and TOI manifest as moving them westward, and the movement is more significant with the development of SAPS during 1800-2200 UT.

3.4 Term analysis during SAPS affecting SED/TOI

To investigate the SAPS-induced electron density disturbances, a term analysis of O^+ continuity equation has been performed in default-TIEGCM and SAPS-TIEGCM, following the method using in previous studies (e.g., Buonsanto et al., 1995; Lei et al., 2008; Liu et al., 2016; and Zhang et al., 2021c). The O^+ continuity equation is expressed as follow

$$\frac{\partial N_{O^+}}{\partial t} = q_{O^+} - \beta N_{O^+} - \nabla \cdot (N_{O^+} \boldsymbol{V}),$$

where N_{O^+}, q_{O^+}, β, and $\boldsymbol{V}$ are the density, chemical production, loss coefficient, and velocity of O^+, respectively. The factors affecting change rate of O^+ density include chemical terms (production and loss) and transport terms which consist of neutral wind transport, electric field transport, and ambipolar diffusion. As O^+ is the major ion species in the F region, the change rate of O^+ density can almost represent the change rate of electron density. Thus, the change rate of electron density, δNE, can be described as

$$\delta \mathrm{NE} = \delta \mathrm{NE}_{\mathrm{ch}} + \delta \mathrm{NE}_{\mathrm{w}} + \delta \mathrm{NE}_{\mathrm{E\times B}} + \delta \mathrm{NE}_{\mathrm{diff}},$$

where $\delta \mathrm{NE}_{\mathrm{ch}}$, $\delta \mathrm{NE}_{\mathrm{w}}$, $\delta \mathrm{NE}_{\mathrm{E\times B}}$ and $\delta \mathrm{NE}_{\mathrm{diff}}$ are the change rate of electron density induced by chemical processes, neutral wind transport, electric field transport, and

ambipolar diffusion, respectively. To compare the relative contributions between these different terms during SAPS affecting SED and TOI, the absolute difference for electron density, neutral temperature, thermospheric composition, chemical and transport terms between SAPS-TIEGCM and default-TIEGCM at 240 km and 390 km are depicted in Figure 5.

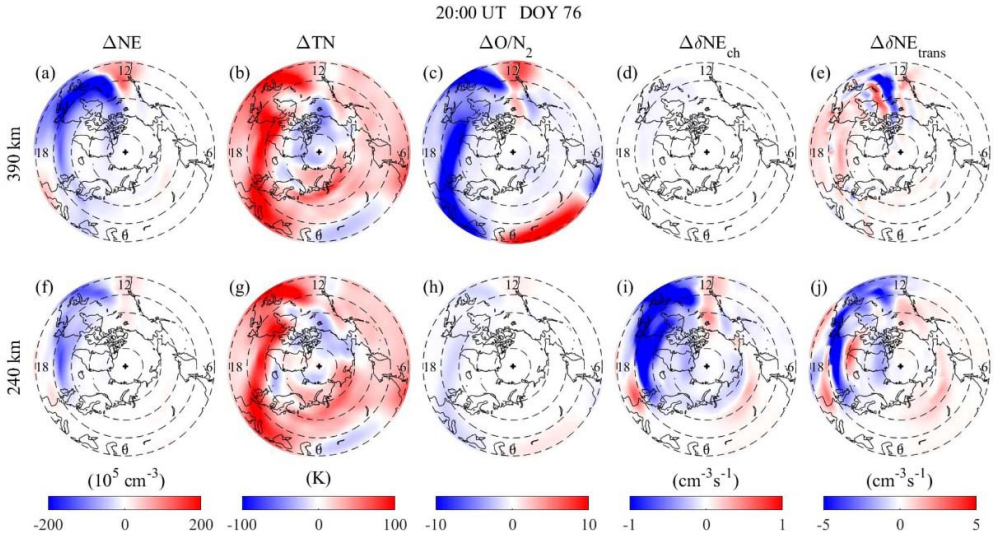

Figure 5. The absolute difference between SAPS-TIEGCM and default-TIEGCM for (a,f) electron density (ΔNE), (b,g) neutral temperature (ΔTN), (c,h) thermospheric composition ($\Delta O/N_2$), electron density change rate induced by (d,i) chemical processes ($\Delta\delta NE_{ch}$), and (e,j) transport processes ($\Delta\delta NE_{trans}$) at 390 and 240 km at 2000 UT.

The simulated F_2 layer peak height (h_mF_2) is ~340 km on average. In Figure 5a, the variation of electron density is significant above h_mF_2. On one hand, the violent frictions between high-speed plasmas and background atmosphere lead to the increases of duskside thermospheric temperature in Figures 5b and 5g, and the increased neutral and plasma temperatures can cause the enhanced recombination rates in Figure 5d and 5i as reported in previous studies (e.g., Foster et al., 2002b; Moffett et al., 1992; Schunk et al., 1975). On the other hand, the local heating in the SAPS region can induce the changes of thermospheric composition in topside F-

region as shown in Figure 5c. The O/N_2 decreases at dusk sector and increases at noon, which indicates that there are upwelling around SAPS channel and downwelling at the westward edge of SAPS. The upward neutral winds lead to a decrease in O/N_2 owing to the uplifting molecular rich air from lower altitudes, and the upwelling with high recombination rate contributes to electron depletion, while the downwelling does the opposite. Wang et al. (2012) also exhibit that SAPS can result in upwelling owing to local Joule heating in the SAPS region and downwelling owing to neutral wind convergent flow away from the SAPS region. Figures 5e and 5j exhibit that SAPS-induced transport processes increase the electron density in the topside ionosphere and decrease the electron density in the bottomside along SAPS channel. The directions of ion vertical transport in SAPS channel roughly consist with neutral winds indicated by Figure 5c. Therefore, the heated plasmas and the upwelling of thermosphere contribute to the increased chemical loss rate in dusk, while the downwelling contribute to the decrease in loss rate at noon.

As the variations of plasma transport shown in Figures 5e and 5j are complex around the westward edge of SAPS, Figure 6 shows the detailed latitude-altitude profiles for electron density and electron density change rate induced by chemical and transport processes in SED region with reduced electron density (1400 LT) and enhanced electron density (1230 LT) at 2000 UT. The absolute differences of neutral winds between SAPS-TIEGCM and default-TIEGCM are shown in Figures 6c and 6j. Since the influences of SAPS on meridional winds are much greater than that on vertical winds, the amplitudes of vertical winds are magnified 10 times for a better visibility. The simulated SAPS was driven by 3-hour Kp index which reached more than 6 at 0600 UT and lasted for 18 hours as shown in Figure 1f, so the SAPS were obviously activated at 0600 UT. At 2000 UT, SAPS significantly enhance the upward and equatorward winds in a wide range in Figure 6c as reported by Wang et al. (2012). In SAPS channel (at 1400 LT), the enhanced upward winds with velocities of ~20 m/s tend to increase the electron density above h_mF_2 and reduce it below h_mF_2 in Figure 6c, and the uplifting of thermosphere with a high

366 recombination rate combined with local heating cause the high loss rate in Figure
367 6b. Meanwhile, SAPS induce weaker downward and poleward winds with velocities
368 of ~5 m/s at its westward edge in Figure 6j, leading to the low loss rate as shown in
369 Figure 6i. However, because the downwelling is so weak at 1230 LT, the dominant
370 westward wind transports still cause the electron density increase above h_mF_2 and
371 decrease below h_mF_2 as the same tendency in SAPS channel at subauroral latitudes
372 in Figure 6j. The SAPS-induced subauroral vertical ambipolar diffusions driven by
373 local Joule heating are consistent with the vertical winds to transport plasma from
374 bottomside of F-region to its topside at 1400 LT, and do the opposite at 1230 LT.
375 The heated plasmas are cooled adiabatically and descend at SAPS equatorward and
376 westward edges (Wang et al., 2012). Moreover, Figure 6f shows that the horizontal
377 electron transport reduces electron density at eastside SED (1400 LT), and enhances
378 density at its westside (1230 LT), which implies that the plasmas are deposited on
379 the westward edge of SAPS and contribute to westside SED. Compared with the
380 weak downwelling leading to the thermospheric composition changes, the horizonal
381 E×B transports should be the main reason for the SAPS-enhanced westside SED.
382

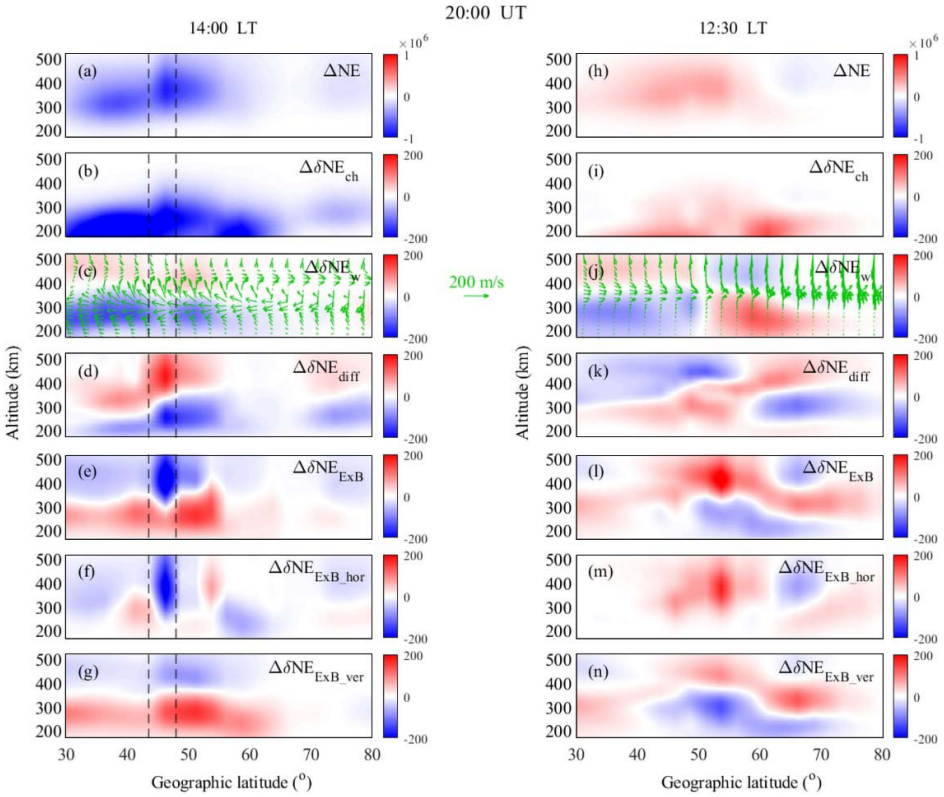

Figure 6. Geographic latitude-altitude profiles of the absolute difference between SAPS-TIEGCM and default-TIEGCM for (a,h) electron density and electron density change rate induced by (b,i) chemical processes, (c,j) neutral winds, (d,k) ambipolar diffusion, (e,l) electric fields, (f,m) horizontal component of electric fields ($\Delta\delta\mathrm{NE}_{\mathrm{E\times B\_hor}}$) and (g,n) vertical component of electric fields ($\Delta\delta\mathrm{NE}_{\mathrm{E\times B\_ver}}$) at 1400 LT and 1230 LT at 2000 UT. The regions between two dashed lines denote the SAPS channel. The green arrows denote SAPS-induced neutral wind disturbances.

4. Discussion

SAPS can affect SED by local heating and ion drag to induce chemical and dynamic processes. Moreover, Figure 6 (e-g and l-n) exhibits that SAPS can also modulate electron density by changing electrodynamic processes, which imply that SAPS can cause electric field variations. The SAPS-induced changes in horizonal neutral winds, ion vertical velocities, and horizonal electric fields are shown in

399 Figure 7.

400

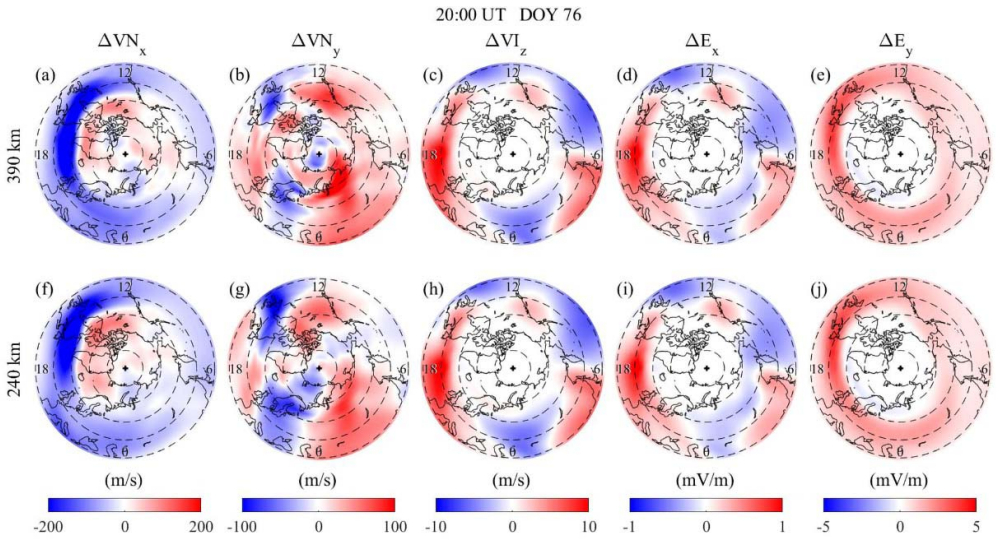

401

402 **Figure 7.** The absolute differences between SAPS-TIEGCM and default-TIEGCM
403 for (a,f) eastward winds (ΔVN_x), (b,g) northward winds (ΔVN_y), (c,h) upward ion E
404 ×B drift velocity (ΔVI_z), (d,i) eastward electric field (ΔE_x), and (e,j) northward
405 electric field (ΔE_y) at 240 and 390 km at 2000 UT.

406

407 Westward SAPS can enhance the local westward neutral winds by ion-neutral
408 collision in Figures 7a and 7f as reported in the literature (e.g., Miller et al., 1990;
409 Reddy and Mayr, 1998; Wang et al., 2012). The enhanced westward winds
410 combined with the downward component of geomagnetic field can promote
411 poleward polarization electric fields through the dynamo process as Figures 7e and
412 7j. As the peak velocity of the modeled SAPS is only ~300 m/s, ΔE_y is just below 5
413 mV/m. Banafsheh et al. (2019) also shows that the neutral wind dynamo effect can
414 increase the ion westward drift by 20% using a MIT coupling model RCM-CTIPe.
415 The enhanced westward E×B transport at westward edge of SAPS redistributes
416 electron density from eastside of SED to its westside as shown in Figures 6f and
417 6m.

418 On the other hand, SAPS-driven meridional winds are more complicated due to

the geomagnetic inclination, LT, and UT by changing the pressure gradient, ion drag, the Coriolis force, and the centrifugal force (Ferdousi et al., 2019; Wang et al., 2012; Zhang et al., 2021a) as shown in Figures 7b and 7g. The meridional wind dynamo process cause the changes in zonal polarization electric field as shown in Figures 7d and 7i, which results in the vertical E×B drifts as shown in Figures 7c and 7h. Wang et al. (2012) disclose that the adiabatic thermal expansion of heated plasma may lead to an upward ambipolar diffusion combined with the upwelling of the thermosphere in SAPS channel. Our results show that vertical E×B drifts induced by the dynamo processes of meridional winds are consisted with ambipolar diffusion to enhance the upward transports in SAPS channel and the downward transports at westward edge of the flow channel.

Overall, the dynamic effects of SAPS in ionosphere-thermosphere system drive not only the changes in plasma chemical processes and thermospheric composition, but also the dynamics and electrodynamics of plasmas to redistribute the electron density in SED and TOI region. The SAPS-induced horizonal transports tends to directly move SED westward, while the vertical transports alter the electron density in SED by affecting plasma temperature via adiabatic compression or expansion processes. Our results prove that the influences of SAPS on SED and TOI depend on their relative locations. SAPS decrease the electron densities in SED and TOI throat region overlapped with SAPS channel, and increase the electron densities in SED located at SAPS westward edge. Therefore, SAPS may be a part of the reason for forming SED at afternoon sector (Evans et al., 1983, Foster et al., 2006; and Pirog et al., 2009). Meanwhile, there is no contradiction between that SAPS weaken SED by reducing electron density along its channel (Fuller-Rowell, 2011) and that SAPS promote SED formation through zonal transport (Foster et al., 2007b).

5. Summary

By imposing a non-self-consistent empirical SAPS model into TIEGCM model, this work investigates the subsequent ionosphere-thermosphere response caused by

high-speed westward plasma flow. Simulated results show that SAPS can significantly impact on the location and strength of SED and TOI by modulating local electron density. The TEC depletion appears in SED region and throat region of TOI overlapped with SAPS channel, while a TEC raise appears at the westward edge of SAPS. As a result, SED and the throat of TOI are forced to shift westward, and the influences of SAPS enter the polar cap with convection to weaken the intensity of TOI.

A term analysis for O^+ to confirm that the major mechanisms in the influences of SAPS on SED and TOI are the variations of ionospheric loss rates and dynamic and electrodynamic transports. In SED and throat of TOI overlapped with high-speed SAPS, the electron density decreases in three ways. (1) The heated plasma by ion-neutral atmosphere friction raises the local loss rate; (2) The upwelling of the thermosphere induced by upward ambipolar diffusion of heated plasma reduce O/N_2 to increase the loss rate; (3) the horizonal E×B transport moves plasma westward out of flow channel. In sunward SED region, SAPS enhance the electron density in two ways. (1) The downwelling driven by adiabatic thermal cooling increases O/N_2 to reduce the loss rate; (2) the plasma transported to the westward edge of SAPS is stacked near noon.

Using SAPS-TIEGCM, this work exhibits the detailed impacts of SAPS on SED and TOI and the physical mechanisms. But due to the differences in SAPS intensity between the results from empirical SAPS model and actual observations, the conclusions in this work are qualitative to some extent.

Acknowledgments

This work is supported by the National Natural Science Foundation of China 42122031, 42074188, and 42004135, the Shandong Provincial Natural Science Foundation ZR2022JQ18, the Chinese Meridian Project and US NSF Awards 1739188, 1522133, AGS1452309, the China Postdoctoral Science Foundation 2020M682465, the Strategic Priority Research Program of Chinese Academy of

Sciences XDB 41000000. We acknowledge the use of data from the Chinese Meridian Project. The solar wind parameters are obtained from the OMNI 2 database (https://spdf.gsfc.nasa.gov/pub/data/omni/high_res_omni/). The TEC and DMSP data can be obtained from the Madrigal database (http://cedar.openmadrigal.org/).

References

Anderson P. C., Hanson W. B., Heelis R. A., et al. (1993), A proposed production model of rapid subauroral ion drifts and their relationship to substorm evolution, *Journal of Geophysical Research: Space Physics*, 98, 6069-6078. doi:10.1029/92JA01975

Banafsheh F., Yukitoshi N., Naomi M., et al. (2019), Subauroral neutral wind driving and its feedback to SAPS during the 17 March 2013 geomagnetic storm. *Journal of Geophysical Research: Space Physics*, 124, 2323-2337. doi:10.1029/2018JA02619

Basu S., Basu S., Rich F. J., et al. (2007), Response of the equatorial ionosphere at dusk to penetration electric fields during intense magnetic storms. *Journal of Geophysical Research: Space Physics*, 112(A8), A08308. doi:10.1029/2006JA012192Buonsanto M. J. (1995), Millstone Hill incoherent scatter F region observations during the disturbances of June 1991, *Journal of Geophysical Research: Space Physics*, 100(A4), 5743-5755. doi:10.1029/94JA03316

Coster A., and Skone S. (2009), Monitoring storm-enhanced density using IGS reference station data, *Journal of Geodesy*, 83(3-4), 345-351. doi: 10.1007/s00190-008-0272-3

Erickson P. J., Beroz F., and Miskin M. Z. (2011), Statistical characterization of the American sector subauroral polarization stream using incoherent scatter radar, *Journal of Geophysical Research: Space Physics*, 116, A00J21.

505 doi:10.1029/2010JA015738
506 Evans, J. V., Holt J. M., Oliver W. L., et al. (1983), The fossil theory of nighttime
507 high latitude F region troughs, *Journal of Geophysical Research: Space*
508 *Physics*, 88, 7769-7782. doi:10.1029/JA088iA10p07769
509 Ferdousi B., Nishimura Y., Maruyama N., et al. (2019), Subauroral Neutral Wind
510 Driving and Its Feedback to SAPS During the 17 March 2013 Geomagnetic
511 Storm, *Journal of Geophysical Research: Space Physics*, 124(3), 2323-2337.
512 doi:10.1029/2018JA026193
513 Foster J. C. (1993), Storm-time plasma transport at middle and high latitudes,
514 *Journal of Geophysical Research: Space Physics*, 98, 1675-1689.
515 doi:10.1029/92JA02032
516 Foster J. C., Burke W. J. (2002a), SAPS: a new categorization for sub-auroral
517 electric fields, *Eos*, 83, 393-394. doi:10.1029/2002EO000289
518 Foster J. C., and Vo H. B. (2002b), Average characteristics and activity dependence
519 of the subauroral polarization stream, *Journal of Geophysical Research: Space*
520 *Physics*, 107(A12), 1475. doi:10.1029/2002JA009409
521 Foster J. C., Coster A. J., Erickson P. J., et al. (2005), Multiradar observations of the
522 polar tongue of ionization, *Journal of Geophysical Research: Space Physics*,
523 110, A09S31. doi:10.1029/2004JA010928
524 Foster J. C., and Rideout W. (2005), Midlatitude TEC enhancements during the
525 October 2003 superstorm. *Geophysical Research Letters*, 32, L12S04.
526 doi:10.1029/2004GL021719
527 Foster J. C., and Rideout W. (2007a), Storm enhanced density: magnetic conjugacy
528 effects, *Annales Geophysicae*, 25(8), 1791-1799. doi:10.5194/angeo-25-1791-
529 2007
530 Foster J. C., Rideout W., Sandel B., et al. (2007b), On the relationship of SAPS to
531 storm-enhanced density, *Journal of Atmospheric and Solar-Terrestrial Physics*,
532 69, 303-313. doi:10.1016/j.jastp.2006.07.021
533 Foster J. C., Erichson P. J., Baker D. N., et al. (2014a), Prompt energization of
534 relativistic and highly relativistic electrons during a substorm interval: Van

Allen Probes observations, *Geophysical Research Letters*, 41(1), 20-25. doi:10.1002/2013GL058438

Foster J. C., Erickson P. J., Coster A. J., et al. (2014b), Storm time observations of plasmasphere erosion flux in the magnetosphere and ionosphere, *Geophysical Research Letters*, 41(3), 762-768. doi:10.1002/2013GL059124

Foster J. C., Zou S. S., Heelis R. A., et al. (2021), Ionospheric Storm-Enhanced Density Plumes, In Ionosphere Dynamics and Applications (eds C. Huang, G. Lu, Y. Zhang and L.J. Paxton). doi:10.1002/9781119815617.ch6

Fuller-Rowell T. J. (2011), Storm-Time Response of the Thermosphere-Ionosphere System. In: Abdu M., Pancheva D, (eds) Aeronomy of the Earth's Atmosphere and Ionosphere, IAGA Special Sopron Book Series, vol 2. Springer, Dordrecht. doi:10.1007/978-94-007-0326-1_32

Galperin Y., Ponomarev V. N., and Zosimova A. G. (1974), Plasma convection in the polar ionosphere, *Annales de Geophysique*., 30, 1-7.

Galperin Y. I., Khalipov V. L., and Filippov V. M. (1986), Signature of rapid subauroral ion drifts in the high-latitude ionosphere structure, *Annales Geophysicae Series A-Upper Atmosphere and Space Sciences*, 4(2), 145-153. doi:10.1029/JB091iB05p05029

Goldstein J., Burch J. L., Sandel B. R., et al. (2015), Coupled response of the inner magnetosphere and ionosphere on 17 April 2002, *Journal of Geophysical Research: Space Physics*, 110(A3), A03205. doi:10.1029/2004JA010712

Hagan M. E., and Forbes J. M. (2002), Migrating and nonmigrating diurnal tides in the middle and upper atmosphere excited by tropospheric latent heat release, *Journal of Geophysical Research: Atmospheres*, 107(D24), 4754. doi:10.1029/2001JD001236

Hagan M. E., and Forbes J. M. (2003), Migrating and nonmigrating semidiurnal tides in the upper atmosphere excited by tropospheric latent heat release, *Journal of Geophysical Research: Space Physics*, 108(A2), 1062. doi:10.1029/2002JA009466

He F., Zhang X. X., Wang W. B., and Wan W. X. (2017). Different evolution

565 patterns of subauroral polarization streams (SAPS) during intense storms and
566 quiet time substorms. *Geophysical Research Letters*, 44, 10796-10804.
567 doi:10.1002/2017GL075449
568 He F., Zhang X. X., Wang W. B., et al. (2018), Large-Scale Structure of Subauroral
569 Polarization Streams During the Main Phase of a Severe Geomagnetic Storm,
570 *Journal of Geophysical Research: Space Physics*, 123(4), 2964-2973. doi:
571 10.1002/2018JA025234
572 Heelis R. A., Lowell J. K., and Spiro R. W. (1982), A model of the high-latitude
573 ionospheric convection pattern, *Journal of Geophysical Research: Space*
574 *Physics*, 87(A8), 6339-6345. doi:10.1029/JA087iA08p06339
575 Horvath I., and Lovell B. C. (2009), Storm-enhanced plasma density features,
576 daytime polar cap plasma enhancements, and their underlying plasma flows
577 investigated during superstorms, *Journal of Geophysical Research: Space*
578 *Physics*, 114, A11304, doi:10.1029/2009JA014465
579 Horvath I., and Lovell B. C. (2014), Large plasma density enhancements occurring
580 in the northern polar region during the 6 April 2000 superstorm, *Journal of*
581 *Geophysical Research: Space Physics*, 119(6), 4805-4818.
582 doi:10.1002/2014JA019917
583 Horvath I., and Lovell B. C. (2016), Structured subauroral polarization streams and
584 related auroral undulations occurring on the storm day of 21 January 2005,
585 *Journal of Geophysical Research: Space Physics*, 121(2), 1680-1695.
586 doi:10.1002/2015JA022057
587 Horvath I., and Lovell B. C. (2020), Investigating Magnetosphere-Ionosphere-
588 Thermosphere (M-I-T) Coupling Occurring During the 7-8 November 2004
589 Superstorm, *Journal of Geophysical Research: Space Physics*, 125(2),
590 e2019JA027484. doi:10.1029/2019JA027484
591 Hosokawa K., Tsugawa T., Shiokawa K., et al. (2010), Dynamic temporal evolution
592 of polar cap tongue of ionization during magnetic storm, *Journal of*
593 *Geophysical Research: Space Physics*, 115, A12333.
594 doi:10.1029/2010JA015848

595 Karlsson T., Marklund G. T., Blomberg L. G., et al. (1998), Subauroral electric
596 fields observed by the Freja satellite: A statistical study, *Journal of Geophysical*
597 *Research: Space Physics*, 103, 4327-4341. doi:10.1029/97JA00333
598 Kunduri B. S. R., Baker J. B. H., Ruohoniemi J. M., et al. (2017). Statistical
599 characterization of the large-scale structure of the sub-auroral polarization
600 stream. *Journal of Geophysical Research: Space Physics*, 122, 6035-6048.
601 doi:10.1002/2017JA024131
602 Lei J. H., Wang W. B., Burns A. G., et al. (2008), Observations and simulations of
603 the ionospheric and thermospheric response to the December 2006 geomagnetic
604 storm: Initial phase, *Journal of Geophysical Research: Space Physics*, 113(A1),
605 A01314. doi:10.1029/2007JA012807
606 Lejosne S., and Mozer F. S. (2017). Subauroral polarization streams (SAPS)
607 duration as determined from Van Allen Probe successive electric drift
608 measurements. *Geophysical Research Letters*, 44, 9134-9141.
609 doi:10.1002/2017GL074985
610 Li W., Thorne R. M., Ma Q., et al. (2014), Radiation belt electron acceleration by
611 chorus waves during the 17 March 2013 storm, *Journal of Geophysical*
612 *Research: Space Physics*, 119(6), 4681-4693. doi:10.1002/2014JA019945
613 Lin D., Wang W. B., Scales W. A., et al. (2019), SAPS in the 17 March 2013 Storm
614 Event: Initial Results From the Coupled Magnetosphere-Ionosphere-
615 Thermosphere Model, *Journal of Geophysical Research: Space Physics*,
616 124(7), 6212-6225. doi:10.1029/2019JA026698
617 Liu J., Nakamura T., Liu L., et al. (2015), Formation of polar ionospheric tongue of
618 ionization during minor geomagnetic disturbed conditions, *Journal of*
619 *Geophysical Research: Space Physics*, 120(8), 6860-6873.
620 doi:10.1002/2015JA021393
621 Liu J., Wang W. B., Burns A., et al. (2016a), Profiles of ionospheric storm-enhanced
622 density during the 17 March 2015 great storm, *Journal of Geophysical*
623 *Research: Space Physics*, 121(1), 727-744. doi:10.1002/2015JA021832
624 Liu J., Wang W. B., Burns A., et al. (2016b), Relative importance of horizontal and

625 vertical transports to the formation of ionospheric storm-enhanced density and
626 polar tongue of ionization, *Journal of Geophysical Research: Space Physics*,
627 121(8), 8121-8133. doi:10.1002/2016JA022882
628 Lu G., Zakharenkova I., Cherniak I., et al. (2020), Large-scale ionospheric
629 disturbances during the 17 march 2015 storm: a model-data comparative study,
630 *Journal of Geophysical Research: Space Physics*, 125(5).
631 doi:10.1029/2019JA027726
632 Miller N. J., Brace L. H., Spencer N. W., et al. (1990), DE 2 Observations of
633 disturbances in the upper atmosphere during a geomagnetic storm, *Journal of*
634 *Geophysical Research: Space Physics*, 95(A12), 21017-21031,
635 doi:10.1029/JA095iA12p21017.
636 Moen J., Oksavik K., Alfonsi L., et al. (2013), Space weather challenges of the polar
637 cap ionosphere, *Journal of Space Weather and Space Climate*, 3, A02.
638 doi:10.1051/swsc/2013025
639 Moffett R. J., Heelis R. A., Sellek R., et al. (1992), The temporal evolution of the
640 ionospheric signatures of subauroral ion drifts, *Planetary and Space Science*,
641 40(5), 663-670. doi:10.1016/0032-0633(92)90007-B
642 Park J., Lühr H., Jakowski N., et al. (2012), A long-lived band of plasma density
643 enhancement at mid-latitudes during the 2003 Halloween magnetic storm,
644 *Journal of Atmospheric and Solar-Terrestrial Physics*, 80, 100-110.
645 doi:10.1016/j.jastp.2012.03.009
646 Pintér B., Thom S. D., Balthazor R., et al. (2006), Modeling subauroral polarization
647 streams equatorward of the plasmapause footprints, *Journal of Geophysical*
648 *Research: Space Physics*, 111(A10), A10306. doi:10.1029/2005JA011457
649 Pirog O. M., Polekh N. M., Romanova E. B., et al. (2009), The main ionospheric
650 trough in the East Asia region: Observation and modeling, *Journal of*
651 *Atmospheric and Solar-Terrestrial Physics*, 71(1), 49-60.
652 doi:10.1016/j.jastp.2008.10.010
653 Reddy C. A., and Mayr H. G. (1998), Storm-time penetration to low latitudes of
654 magnetospheric-ionospheric convection and convection-driven thermospheric

winds, *Geophysical Research Letters*, 25(16), 3075-3078, doi:10.1029/98GL02334.

Rich F. J., and Hairston M.J. (1994), Large-scale convection patterns observed by DMSP, Journal of Geo*physical Research*, 99(A3), 3827-3844. doi: 10.1029/93JA03296

Richards P. G., Fennelly J. A., and Torr D. G. (1994), EUVAC: A solar EUV flux model for aeronomic calculations, *Journal of Geophysical Research: Space Physics*, 99(A5), 8981-8992. doi:10.1029/94JA00518

Rideout W., and Coster A. (2006), Automated GPS processing for global total electron content data, *GPS Solutions*, 10(3), 219-228. doi:10.1007/s10291-006-0029-5

Roble R. G., and Ridley E. C. (1987), An auroral model for the NCAR thermospheric general circulation model (TGCM), *Annales Geophysicae Series A-Upper Atmosphere and Space Sciences*, 5(6), 369-382.

Schunk R.W., Raitt W. J., Banks P. M. (1975), Effect of Electric-Fields on Daytime High Latitude E and F Regions, *Journal of Geophysical Research: Space Physics*, 80(22), 3121-3130. doi:10.1029/JA080i022p03121

Sellek R., Bailey G. J., Moffett R. J., et al. (1991), Effects of large zonal plasma drifts on the subauroral ionosphere, *Journal of Atmospheric and Terrestrial Physics*, 53(6-7), 557-565. doi:10.1016/0021-9169(91)90083-J

Smiddy M., Kelley M. C., Burke W., et al. (1977), Intense poleward directed electric fields near the ionospheric projection of the plasmapause, *Geophysical Research Letters*, 4, 543-546. doi:10.1029/GL004i011p00543

Southwood D. J., and Wolf R. A. (1978), An assessment of the role of precipitation in magnetospheric convection, *Journal of Geophysical Research: Space Physics*, 83, 5227-5232. doi:10.1029/JA083iA11p05227

Spiro R. W., Heelis R. H., and Hanson W. B. (1979), Rapid sub-auroral ion drifts observed by Atmospheric Explorer C, *Geophysical Research Letters*, 6, 657-660. doi:10.1029/GL006i008p00657

Sun Y. Y., Matsuo T., Araujo-Pradere E. A., et al. (2013), Ground-based GPS

observation of SED-associated irregularities over CONUS, *Journal of Geophysical Research: Space Physics*, 118(5), 2478-2489. doi: 10.1029/2012JA018103

Tu J. N., Song P., and Reinisch B. W. (2008), On the concept of penetration electric field, *AIP Conference Proceedings*, 974, 81-85. doi:10.1063/1.2885036

Vasyliunas V. M. (2001), Electric field and plasma flow: What drives what? *Geophysical Research Letters*, 28(11), 2177-2180. doi:10.1029/2001GL013014

Wang W. B., Talaat E. R., Burns A. G., et al. (2012), Thermosphere and ionosphere response to subauroral polarization streams (SAPS): Model simulations, *Journal of Geophysical Research: Space Physics*, 117(A7), A07301. doi:10.1029/2012JA017656

Weimer D. R. (2005), Improved ionospheric electrodynamic models and application to calculating Joule heating rates, *Journal of Geophysical Research: Space Physics*, 110(A5), A05306. doi:10.1029/2004JA010884

Wolf R. A., Spiro R. W., Sazykin S., et al. (2007), How the Earth's inner magnetosphere works: An evolving picture, *Journal of Atmospheric and Solar-Terrestrial Physics*, 69, 288-302. doi:10.1016/j.jastp.2006.07.026

Wu Q., Sheng C., Wang W. B., et al. (2019), The Midlatitude Thermospheric Dynamics From an Interhemispheric Perspective, *Journal of Geophysical Research: Space Physics*, 124(10), 7971-7983. doi:10.1029/2019JA026967

Yu Y. Q., Jordanova V., Zou S. S., et al. (2015), Modeling subauroral polarization streams during the 17 March 2013 storm, *Journal of Geophysical Research: Space Physics*, 120(3), 1738-1750. doi:10.1002/2014JA020371

Zhang K. D., Wang H., Wang W. B., et al. (2021a), Nighttime meridional neutral wind responses to SAPS simulated by the TIEGCM: A universal time effect, *Earth and Planetary Physics*, 5(1), 52-62. doi:10.26464/epp2021004

Zhang, K. D., Wang, H., Yamazaki, Y., et al. (2021b), Effects of subauroral polarization streams on the equatorial electrojet during the geomagnetic storm on June 1, 2013, *Journal of Geophysical Research: Space Physics*, 126, e2021JA029681. doi:10.1029/2021JA029681

715 Zhang, K. D., Wang, H., Liu, J., et al. (2021c). Dynamics of the tongue of
716 ionizations during the geomagnetic storm on September 7, 2015, *Journal of*
717 *Geophysical Research: Space Physics*, 126, e2020JA029038.
718 doi:10.1029/2020JA029038
719 Zhang, K. D., Wang, H., and Yamazaki, Y. (2022). Effects of subauroral polarization
720 streams on the equatorial electrojet during the geomagnetic storm on 1 June
721 2013: 2. Temporal variations. *Journal of Geophysical Research: Space Physics*,
722 127, e2021JA030180. doi:10.1029/2021JA030180
723 Zhang S. R., Zhang Y. L., Wang W. B., et al. (2017), Geospace system responses to
724 the St. Patrick's Day storms in 2013 and 2015, *Journal of Geophysical*
725 *Research: Space Physics*, 122(6), 6901-6906. doi:10.1002/2017JA024232
726 Zheng Y. H., Brandt P. C., Lui A. T. Y., et al. (2008), On ionospheric trough
727 conductance and subauroral polarization streams: Simulation results, *Journal of*
728 *Geophysical Research: Space Physics*, 113(A4), A04209.
729 doi:10.1029/2007JA012532
730 Zou S. S., Lyons L. R., Wang C. P., et al. (2009), On the coupling between the
731 Harang reversal evolution and substorm dynamics: A synthesis of SuperDARN,
732 DMSP, and IMAGE observations, *Journal of Geophysical Research: Space*
733 *Physics*, 114, A01205. doi:10.1029/2008JA013449
734 Zou S. S., Ridley A. J., Moldwin, M. B., et al. (2013), Multi-instrument
735 observations of SED during 24-25 October 2011 storm: Implications for SED
736 formation processes, *Journal of Geophysical Research: Space Physics*, 118(12),
737 7798-7809. doi:10.1002/2013JA018860
738 Zou S. S., Moldwin, M. B., Ridley, A. J., et al. (2014), On the generation/decay of
739 the storm-enhanced density plumes: Role of the convection flow and field-
740 aligned ion flow, *Journal of Geophysical Research: Space Physics*, 119(10),
741 8543-8559. doi:10.1002/2014JA020408
742

Figure 1.

DOY 75-77

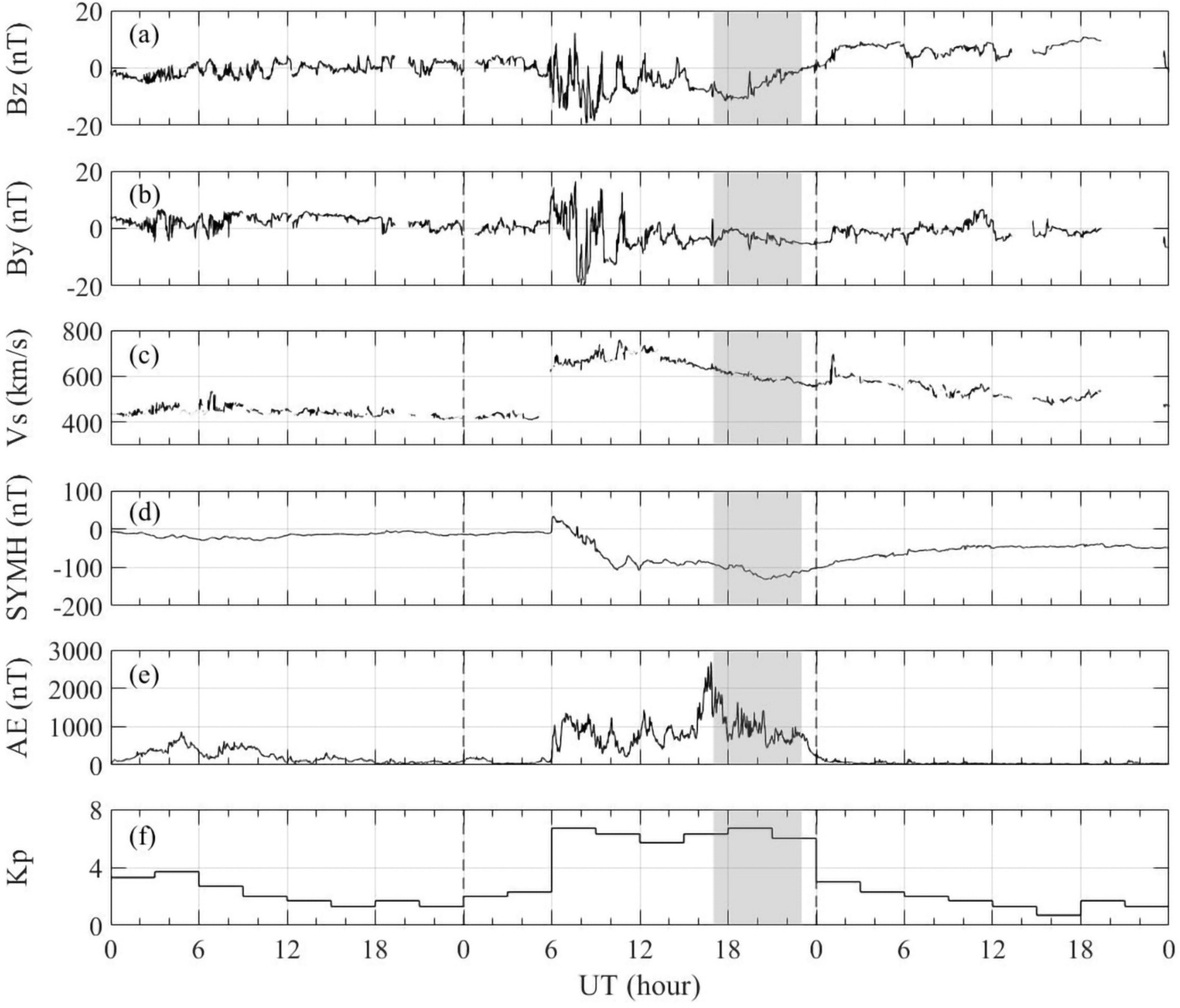
(a)
Bz (nT)
20
0
-20
(b)
By (nT)
20
0
-20
(c)
Vs (km/s)
800
600
400
(d)
SYMH (nT)
100
0
-100
-200
(e)
AE (nT)
3000
2000
1000
0
(f)
Kp
8
4
0
0
6
12
18
0
6
12
18
0
6
12
18
0
UT (hour)

Figure 2.

16:00 UT
18:00 UT
20:00 UT
22:00 UT
GNSS
SAPS-TIEGCM
default-TIEGCM
(a)
(b)
(c)
(d)
(e)
(f)
(g)
(h)
(i)
(j)
(k)
(l)
12
6
0
18
ΔTEC (TECU)
-10
-5
0
5
10

Figure 3.

22:00 UT

(a)

default-TIEGCM

(b)

SAPS-TIEGCM

12

18

6

0

v_i (km/s)

1

0.8

0.6

0.4

0.2

0

-0.2

-0.4

-0.6

-0.8

-1

(c)

v_i (km/s)

2

1.5

1

0.5

0

-0.5

-1

-1.5

-2

21:40

21:45

21:50

21:55

22:00

22:05

22:10

UT

DMSP F17

default-TIEGCM

SAPS-TIEGCM

Figure 4.

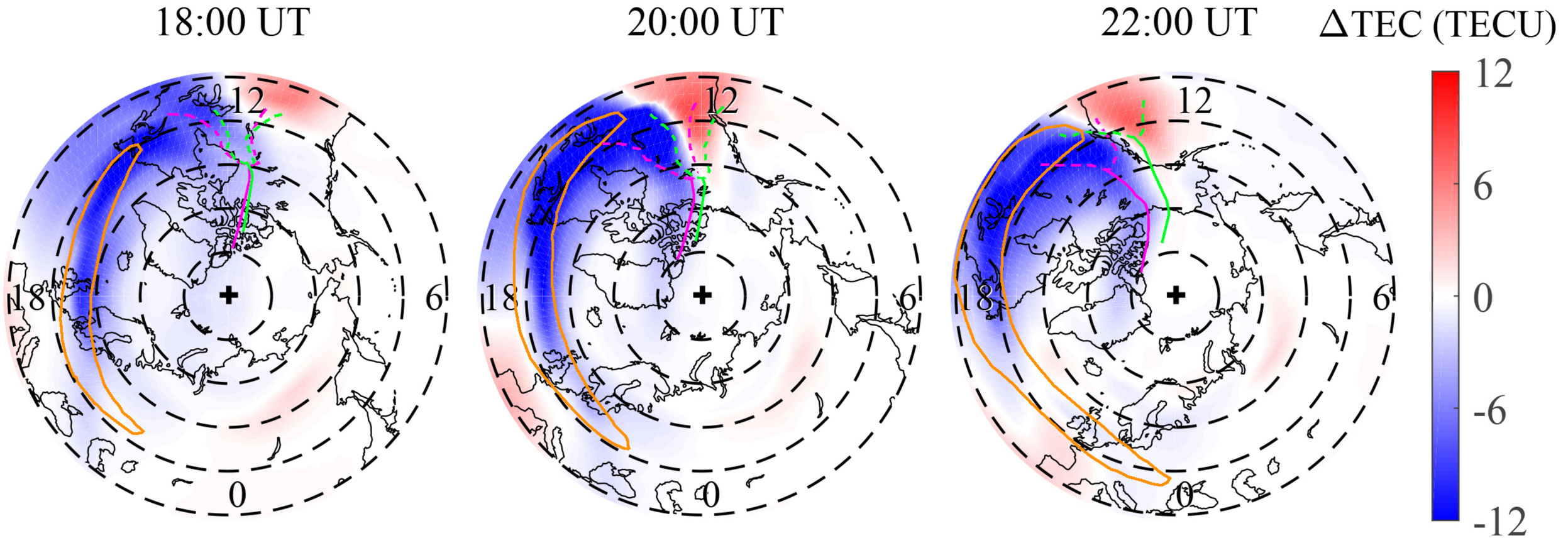
18:00 UT
20:00 UT
22:00 UT
ΔTEC (TECU)
12
6
0
-6
-12
18
6
12
0
18
6
12
0
18
6
12
0

Figure 5.

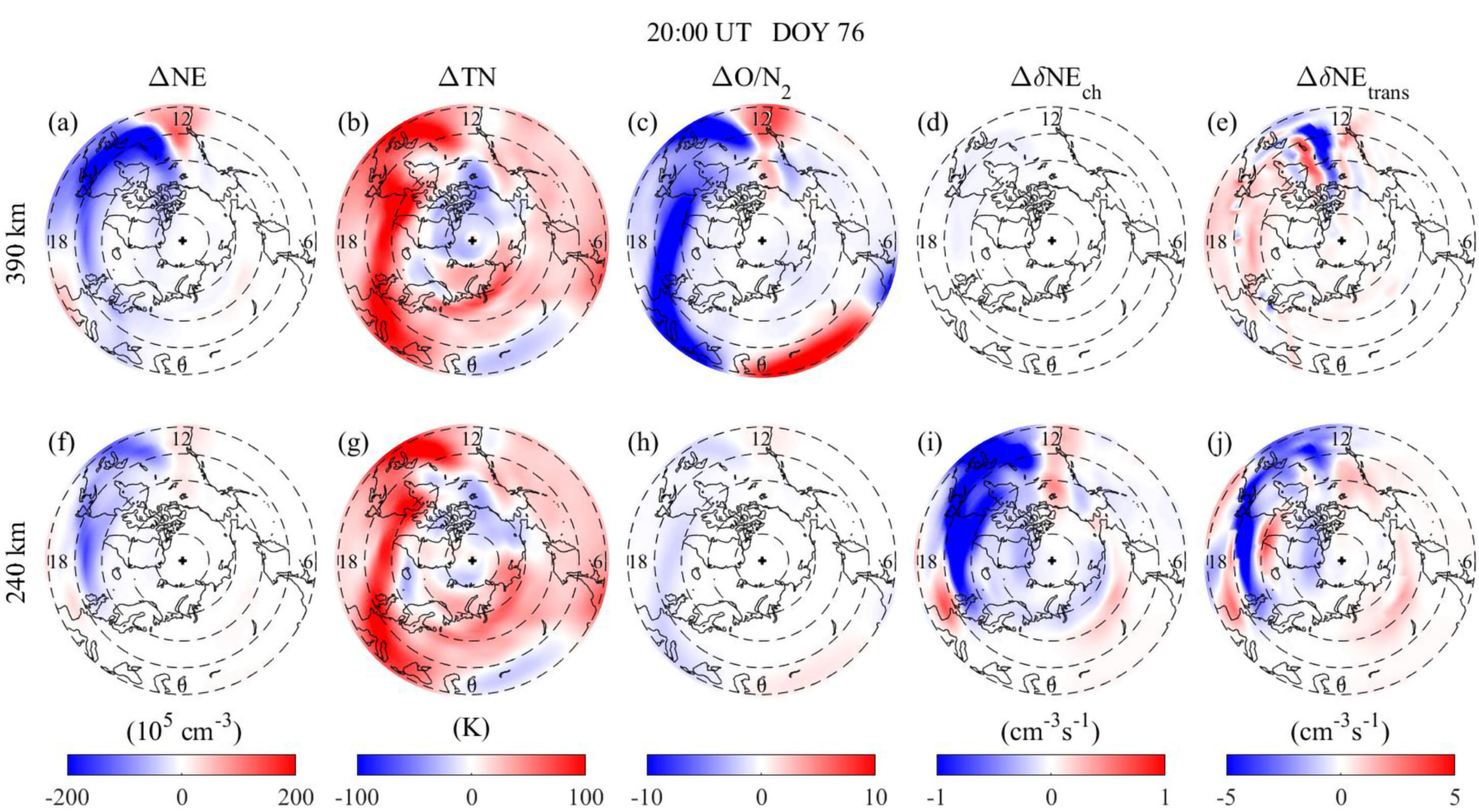
20:00 UT DOY 76
ΔNE
ΔTN
ΔO/N2
ΔδNEch
ΔδNEtrans
390 km
240 km
(a)
(b)
(c)
(d)
(e)
(f)
(g)
(h)
(i)
(j)
12
18
6
θ
(10^5 cm^-3)
-200
0
200
(K)
-100
0
100
-10
0
10
(cm^-3s^-1)
-1
0
1
(cm^-3s^-1)
-5
0
5

Figure 6.

20:00 UT

14:00 LT

12:30 LT

(a) ΔNE

(b) $\Delta\delta NE_{ch}$

(c) $\Delta\delta NE_{w}$

(d) $\Delta\delta NE_{diff}$

(e) $\Delta\delta NE_{ExB}$

(f) $\Delta\delta NE_{ExB\_hor}$

(g) $\Delta\delta NE_{ExB\_ver}$

(h) ΔNE

(i) $\Delta\delta NE_{ch}$

(j) $\Delta\delta NE_{w}$

(k) $\Delta\delta NE_{diff}$

(l) $\Delta\delta NE_{ExB}$

(m) $\Delta\delta NE_{ExB\_hor}$

(n) $\Delta\delta NE_{ExB\_ver}$

200 m/s

$\times 10^6$

1

0

-1

200

0

-200

Altitude (km)

500

400

300

200

30 40 50 60 70 80

Geographic latitude (°)

Figure 7.

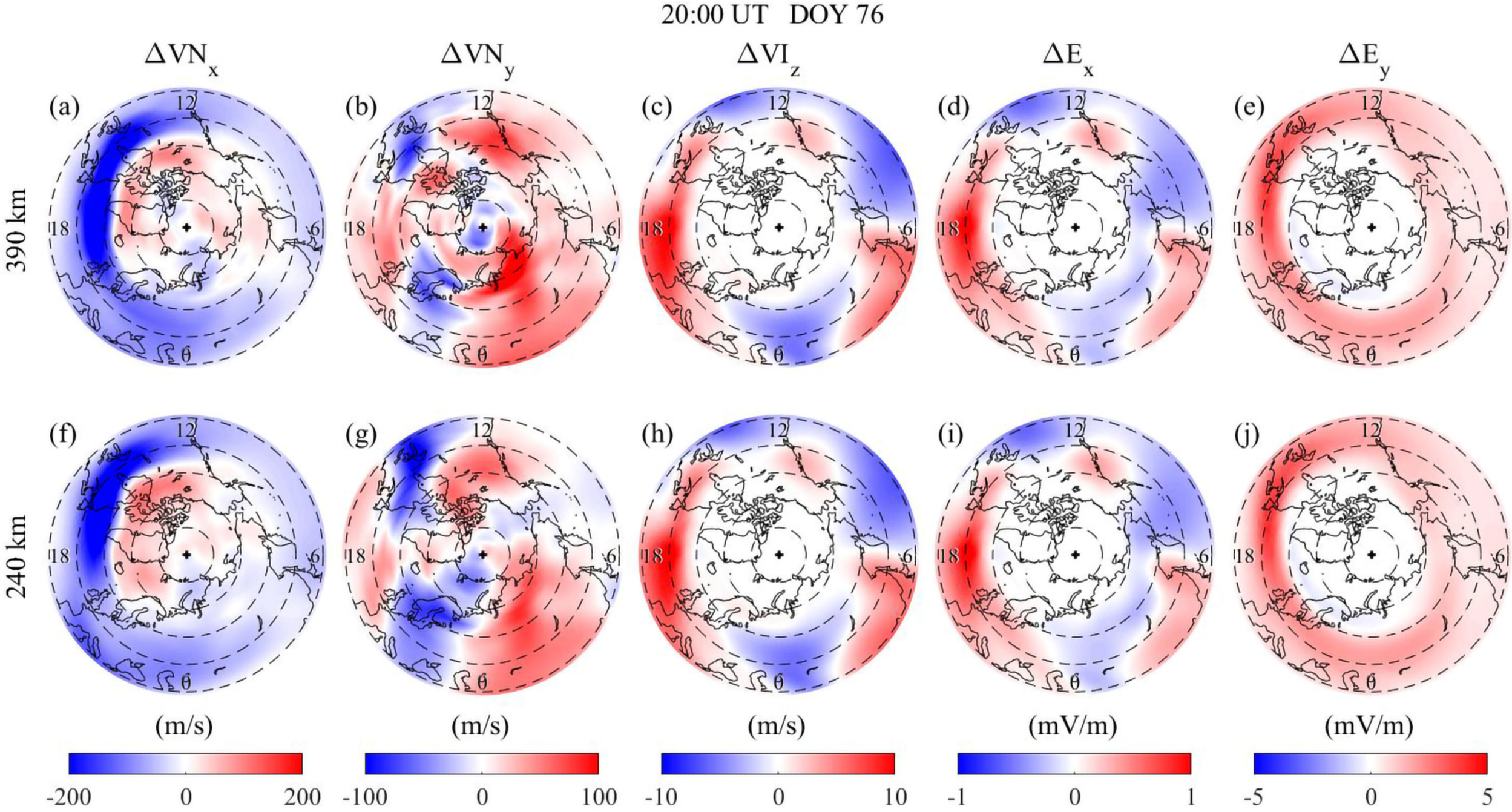
20:00 UT DOY 76
ΔVN x
ΔVN y
ΔVI z
ΔE x
ΔE y
390 km
240 km
(a)
(b)
(c)
(d)
(e)
(f)
(g)
(h)
(i)
(j)
12
18
6
θ
(m/s)
(m/s)
(m/s)
(mV/m)
(mV/m)
-200
0
200
-100
0
100
-10
0
10
-1
0
1
-5
0
5